Chapter

Numerical Simulation of Base Pressure and Drag of Space Reentry Capsules at High Speed

Rakhab C. Mehta

Abstract

The numerical simulations over several reentry vehicles are carried out by solving time-dependent compressible laminar axisymmetric Navier-Stokes equations for Mach 1.2–6.0. The fluid dynamics equations are discretized in spatial coordinates using integral formulation in conjunction with a finite volume method which reduce to semi-discretized ordinary differential equations. A local time-step is used to achieve steady-state solution. The numerical computation is carried out on a single-block structured computational grid. The flowfield features over the reentry vehicle such as formation of a bow shock wave ahead of the fore-body, expansion fan on the shoulder, and recirculation zone in the base region are well captured in the numerical simulations. Lower pressure acting on the base of the reentry capsule acts as base drag. The base drag coefficient based on maximum cross-section of the reentry capsule must satisfy inequality. The base drag coefficient is a function of several geometrical parameters of the fore-body and back-shell of reentry capsule, boundary layer, formation of free-shear layer in the wake region and freestream Mach number. The purpose of this chapter is to numerically evaluate and tabulate the base pressure and the base drag coefficients of various reentry space capsules at zero angle of incidence.

Keywords: aerodynamic, base drag, CFD, high speed flow, viscous flow, reentry vehicle, shock wave

1. Introduction

A space vehicle may be designed with several trajectory options such as non-lifting (steep or shallow), lifting (skipping or diving), terminal (gravity assist), thrusting (jet-on) reentry. The base pressure and heat flux are of paramount importance for smooth deployment of parachute and successful landing of a spacecraft. Cassanto [1] has carried out a number of wind tunnel and free-flight experiments to obtain the base pressure. Lamb et al. [2] have reviewed the base pressure on the reentry vehicle at high speed, which depends on wake flow characteristic, freestream conditions and edge properties of boundary layer at the shoulder of the module. The base pressure correlation for supersonic flows are compared by Kawecki [3] using the ground test data and with different vehicles such as ABC, MK-3, 4, 12, MTV, reentry F, REX, RVTO, SAMAST, TVX and WAC. A supersonic analysis of the SPR INT blunted cone-flare is carried out by Terry and Barber [4] employing computational fluid dynamics (CFD) method as well as wind-tunnel

testing at Mach 3. Experimental and numerical computations by Togiti et al. [5] of the flow behind a truncated cylinder in a supersonic flow reveals almost constant base pressure coefficient. Base flow investigation of the Apollo AS-202 is presented in detail by Walpot et al. [6].

The bow shock wave is formed ahead the blunt body which is enclosed by a subsonic-supersonic region between the blunt body and the bow shock wave. The wall pressure distribution, the location of the sonic line and shock stand-off distance on the spherical cap region have been analytically analyzed by Chester [7] and Freeman [8] at very high speeds with an adiabatic index near to unity which predicts a singular point at 60° from the stagnation point. However, the analytical approach [9] for the high-speed flow over the blunt-body is found to be the most difficult and complex. The flowfield over the reentry capsule becomes further complicated due to the presence of bevel at the shoulder and shape of the base shell of the reentry module.

Aerodynamic analyses of the COMmercial Experiment Transport (COMET) reentry capsule have been carried out by Wood et al. [10] solving the thin layer laminar Navier-Stokes at high speeds. Yamamoto and Yoshioka [11] have performed flowfield computation over the Orbital Reentry EXperiments (OREX) using CFD method in conjunction with flight aerodynamic data. Ivanov [12] cataloged different shapes for non-winged reentry vehicles. The aerodynamic characterization of the CARINA reentry module in the low supersonic Mach regimes has been performed employing numerical and experimental methods [13]. The flowfield simulations over the Beagle-2 spacecraft have been obtained by Liever et al. [14] using CFD code for low supersonic to hypersonic speeds. Mehta [15] has numerically simulated flowfield over atmospheric reentry demonstrator (ARD) and space recovery experiment (SRE).

Wind tunnel testing of the orion crew module (OCM) has been carried out by Ross et al. [16] to obtain the aerodynamic forces. Murphy et al. [17] have presented experimental static aerodynamic data for the OCM reentry capsule and analyzed with the help of surface flow visualization and computational results. Shape optimization design method has been presented by Zhenmiz et al. [18] for the conceptual design of reentry capsules. Ali et al. [19] have studied effects of nose-bluntness ratio on the aerodynamic performance of reentry capsules. CFD analyses of space vehicle are performed employing H3NS and FLUENT code by Viviani et al. [20] to analyze the flowfield over various capsules. Chen et al. [21] have carried out numerical simulations of flowfield for aerodynamic design of reentry capsules. Weiland [22] has presented aerodynamic characteristics of several non-winged capsules. Effects of geometrical parameters over fore-body of various reentry vehicles have been numerically investigated at high speeds [23, 24].

The flowfield feature of shock wave interaction over a double-cone module includes a local flow separation attributed to the semi-cone angle of the double-cone configuration. It has been also observed that these flowfields are controlled by the vorticity in the incoming boundary layer and the strength and the orientation of the shock wave. Numerical and experimental studies have been performed by many researchers [25–27].

It is worth to mention here that considerable difficulties encountered for obtaining aerodynamic data from wind-tunnel testing are attributed to model-sting interference effects. The shock tunnel is having short duration of testing time. In free flight experiments, a scaled model is launched inside a range and orthogonal shadowgraphs are taken as the capsule flies by each shadow graph station. The CFD approach provides flowfield behaviour and aerodynamic coefficients without the sting interference effect. In the present Chapter, numerical studies were undertaken for a freestream Mach number range of 1.2–6.0. The numerical simulation is to solve

the axisymmetric laminar compressible Navier-Stokes equations on a single-block structured grid, i.e., the number of grid points in the radial direction in each zone of the computational region is same. Surface pressure variations over the vehicles are computed which reveal a systematic understanding of the flow features over the capsule at high speeds. It also reveals the effect of geometrical parameters on aerodynamic base drag coefficient. The unsteady flow characteristics of the OREX and the Beagle-2 are analyzed in Ref. [28].

2. Review of the base pressure data

A base pressure experiment for determining the atmospheric pressure profile of planets applicable for Mars, Venus and Jupiter entry probe is presented by Cassanto [29]. The results of a reentry vehicle flight test have demonstrated by Nieden et al. [30] for feasibility of the experiment to obtain the atmospheric pressure profile. The fore-body shape of the reentry vehicle affects the base pressure [31]. Cassanto [32] wind-tunnel data with a sting attached to a model at Mach 4 predict 25–50% higher than the flight data. The Euler code (SAN DIAC) has been employed to compute flowfield over a large number of space vehicles by Noack et al. [33]. Comparisons were made between numerical and experimental results by McWherter et al. [34] using parabolized Navier-Stokes code SPRINT.

Theoretical studies of the fluid dynamics in the base flow region of the vehicle were presented by Baum [35]. They found in the analysis that the outside flow M > 1 is distinguished from relative low velocity core M < 1 of the base flow regimes by a separated flow.

The base pressure for sphere-cone configuration [36] at zero angle of attack was found to be a strong function of cone-angle and bluntness ratio. Analysis of flight-test base pressure data [37] for 10° sharp-cone has shown radial base pressure gradient in laminar flow. It is experimentally found that the base pressure is function of Reynolds number under laminar flow condition. Cassanto et al. [38] have investigated local flow effects on base pressure for the 10° sharp-cone configurations. Free-flight base pressure obtained using telemetry technique was compared with the sting-supported wind-tunnel data at Mach 4. Effects of Mach number on ratio of the base to freestream pressure (p_B/p_∞) in laminar and turbulent case are carried out in wind-tunnel and free-flight testing [38]. Correlation of free-flight base pressure data for Mach 4–19 has been obtained by Cassanto et al. [39]. After-body configuration [40] affects the base pressure ratio levels by about 25% compared to experimental studies. Base pressure measurements on slender cones at zero angle of attack with laminar flow condition on after-body were presented for Mach 11.9. Full-scale flight test base pressure results for a blunt planetary entry probe configuration having a blunt body 52° sphere-cone are analyzed by Cassanto [29]. The base pressure experiment is applicable for Mars, Venus, Jupiter reentry probe missions. The base pressure measurements on a 9° semi-cone angle at Mach range of 3.50–9.20 have been carried out by Zarin [41]. Flight-test base pressure measurements were conducted by Bulmer [42] for Mach number range of 0.5–15. The shapes of the Viking, Mars Path Finder (MPF), Mars Exploration Rovers (MER), Phoenix, Mars Science Laboratory (MSL), Mu-Science Engineering Satellite (MUSES-C) are similar to the Apollo capsule [43]. Aeroassist Flight Experiment (AFE) configurations have been analyzed numerically using two different Navier-Stokes flow solvers by Venkatapathy et al. [44]. The effect of base flow at low supersonic speeds on the sonic line location at hypersonic speed on aerodynamic coefficients has been analyzed by Gnoffo et al. [45]. Tam [46] and Menne [47] have computed flowfield over Viking, Bioconic and AFE vehicles employing Euler flow solver. A spherical

blunt-cone/flare delft aerospace recovery test (DART) configuration is numerically analyzed by Otten [48] solving a laminar Navier-Stokes equations. Numerical analysis over blunted cone flare has been carried out at Mach 6 by Savino et al. [49]. Barnhardt [50] has carried out numerical simulation of flowfield in the wake region of a reentry vehicle at high speeds. The EXPeriment and Recovery of Space System (EXPRESS) reentry capsule at transonic and supersonic speeds is studied experimentally by Suzuki, and Abe [51].

It is important to state here that the base pressure can never be less than zero. The base pressure coefficient can be expressed as

$$C_{PB} = \frac{-p_\infty}{\frac{1}{2}\rho_\infty V_\infty^2}\left(1 - \frac{p_B}{p_\infty}\right) \tag{1}$$

Lower pressure is acting on the base experiences another form of aerodynamic base drag. The base drag coefficient based on the maximum cross-section of the reentry space capsule must satisfy inequality

$$C_{DB} < \frac{2}{\gamma M_\infty^2} \tag{2}$$

Thus, it can be noticed that the base pressure is having complex flow features which are a function of several variables such as geometrical parameters of the fore- and after-body of the reentry space vehicle, Mach number and Reynolds number. The measurements of base pressure in the wind-tunnel testing are affected by the presence of the sting attachment to the model. The free-flight experiment needs pneumatic launcher mechanism, pressure transducer, motion picture photography equipment, antenna, receiver and recording devices. However, the base pressure data obtained from the free-flight experiments are not affected by the sting attachment to the model as in the wind-tunnel testing. The numerical simulations are most suitable and inexpensive tool to evaluate flow characteristics, base pressure and drag coefficient for wide range of Mach numbers and Reynolds numbers.

3. Glimpse of flowfield over reentry vehicles

The flowfield features over the reentry capsule can be delineated through the experimental and theoretical investigations at high speed. The nomenclature and geometrical parameters of a typical reentry capsule is depicted in **Figure 1(a)** that leads to the necessity to investigate the influence of the geometrical parameters such as D, α_N, R_C, α_B, and L on the flowfield and aerodynamic characteristics. A schematic sketch of flowfield is delineated in **Figure 1(b)** based on shadowgraph and schlieren pictures. The significant flow features are described by the following. In the fore-body section of the capsule, the fluid decelerates through the bow shock wave depending on the cruise speed and altitude. At the shoulder of the capsule, the flow turns and expands rapidly and boundary layer detached, forming a free-shear layer in the back-shell region that separates the inner recirculating flow region behind the module from the outer inviscid flowfield. The latter is recompressed and turned back to the freestream direction, first by the so-called lip shock wave, and further downstream by the recompression shock wave. At the end of the recirculating flow past the neck, the free-shear layer develops in the wake trail. A complex flow structure often includes a lip shock wave associated with the beveled expansion fan and wake trail adjacent to the shear layer confluence. The corner expansion process is an expansion fan pattern changed by the presence of the approaching boundary layer and radius of the bevel or shoulder, R_C. The wake flow features

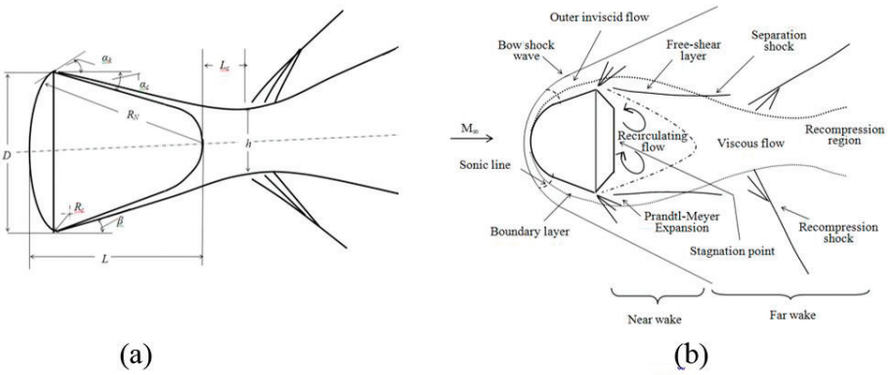

Figure 1.
Representation (a) geometrical parameters (b) flow features.

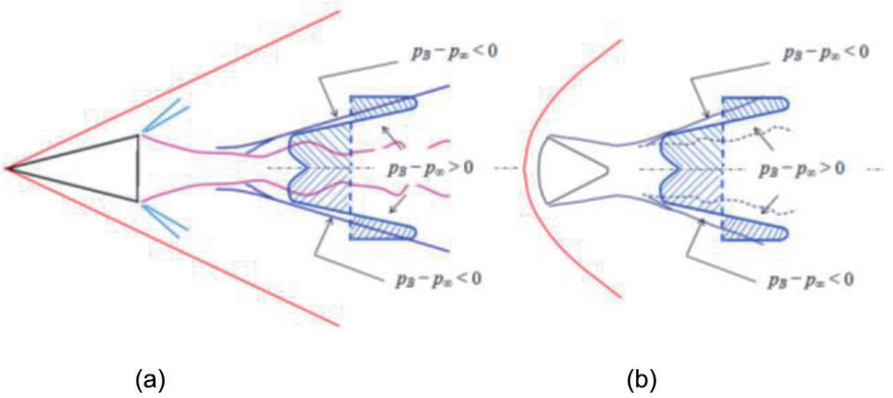

Figure 2.
Illustrations of flowfield over (a) cone (b) space vehicle at M_∞ = 3.1.

show several flowfield features such as free-shear layers, contraction of flow (neck) region and recompression shocks. The base flowfields also exhibit near and far wake region as depicted in **Figure 1(b)**. The values of L_c and h as depicted in **Figure 1(a)** are function several flow variables as mentioned above. The base plane of the capsule experiences another stagnation point.

Figure 2(a) and **(b)** has been drawn with the help of shadowgraph pictures of a 12.5° semi-cone and a blunt body capsule at high speed. The base pressure profile is illustrated in the wake region of the space vehicles. The schematic sketches as shown in **Figure 2** delineate a complex flowfield features associated with the nonlinear base pressure variations in the wake region.

4. Geometrical parameters of reentry vehicles

A high-speed flow past a reentry capsule forms a bow shock wave which causes a high surface pressure. It yields high aerodynamic drag (ballistic coefficient) force, which is needed for aero-braking purposes. Therefore, the primary design consideration of the reentry capsules requires large spherical nose radius R_N and fore-body diameter D as shown in **Figure 1(a)**. Reentry capsule configurations significantly differ from each other due to entry conditions and mission requirements. The sphere space capsule (Sputnik) permits the highest possible volumetric efficiency but does not give good maneuvering ability. Therefore, the reentry space vehicle requires a back-shell with an inclination in order to generate lift to reduce 'g' forces on the crew tolerance levels. Bedin et al. [52] have illustrated sixteen types of space vehicles in which the frontal diameter D of the capsule is kept constant for all configurations

and varying geometrical parameters α_N, R_C, α_B, and L in three groups. Experimental investigation of various combination of cone-segment bodies and spheres of Russian reentry capsules are carried out by Bedin et al. [52] in a pressure-tight ballistic range for ratio of specific heats of 1.14–1.67, Mach number varied from 0.5 to 10, and Reynolds number based on the base diameter varied from 2.5×10^5 to 5.0×10^6.

In the first group, five capsules are having variation in the back-shell angle α_B in the range of 0–30°. In the second group, five capsules are having variation of the overall length varied from 1.0 D to 0.375 D. In the last group the back-shell angle α_B, overall length L, and shoulder radius R_C, alignment with frontal cap are varied to evaluate the ballistic performance. Recently Minenkol et al. [53] have studied the effect of geometrical parameters on aerodynamic performance of the space vehicles such as the Apollo and the Soyuz.

The reentry capsules can be classified as a head-light shape as in the case of Soyuz, or bell shape as in the case of Apollo and ARD, or a saucer type as in the case of OREX. **Table 1** depicts the dimension of the Apollo, the OREX and the Soyuz capsules to emphasis the classification of the capsules based on L/D ratio. The nominal OCM geometry, based on the Apollo configuration, consists of a spherical fore-body transitioning to a conical back-shell section with a truncated base to accommodate docking hardware. The aerodynamic characteristic of the Orion is analyzed numerically and experimentally by Stremel et al. [54]. The OCM is similar in shape to the Apollo Command Module but is approximately 29% larger by length. The ARD resembles a 70% scaled version of Apollo capsule as mentioned by Walpot [6].

The schematic sketches of flowfield feature of the Apollo, the Soyuz, the OREX capsules are displayed in **Figure 3(a)–(c)**. The Apollo and the Soyuz configurations are having spherical-blunt nose segment. The fore-body of the OREX consists of spherical cap with a cone section. The bow shock wave is detached on the blunt fore-body in the case of SRE as delineated in **Figure 3(d)**. The fore-body of the SRE is having a mixed subsonic-supersonic region as seen in the figures. The flowfield in the wake region is affected due to the presence of the truncated cylinder. **Figure 3(e)** shows schematic flowfield features at high speed on a sharp-tipped double-cone configuration. The double cone capsule shows formation of an attached conical shock wave on the tip of the cone. The flowfield in the wake region of a reentry capsule is again found to be complex in nature and is attributed to the expansion fan at corner of the shoulder.

Figure 4 shows the nomenclature of the geometrical parameters of the ARD, the Soyuz, the OREX, the SRE and the double cone reentry capsules. The Soyuz, the Apollo and the OREX capsules are having back-shell inclination angle α_B of 9, 33 and 15° relative to the vehicle's axis of symmetry respectively. **Figure 5** depicts the geometrical details of the CARINA [13] and Beagle-2 [14] capsules. **Table 2** depicts the geometrical detail of Viking, MPF, MER, Phoenix and MSL which are having a 70° sphere-cone shaped (Mars space vehicles) with a back-shell needed for high-speed entry phase and a disk-gap band (DGB) type of supersonic parachute during the descent portion of the entry sequence. **Table 3** presents the dimensional details of the ARD, the Apollo, the OREX, the CARINA, the MUSES-C and the Beagle-2. **Table 4** depicts the dimensional details of the SRE capsule.

Capsule	R_N	D	R_C	L	$\alpha_N{}^0$	$\alpha_B{}^0$
Apollo	4.595	3.95	0.186	2.04	—	33.0
OREX	1.35	3.40	0.001	1.508	50.0	15.0
Soyuz	2.235	2.2	0.014	2.142	—	7.0

Table 1.
Dimension of the Apollo, the OREX and the Soyuz reentry capsules.

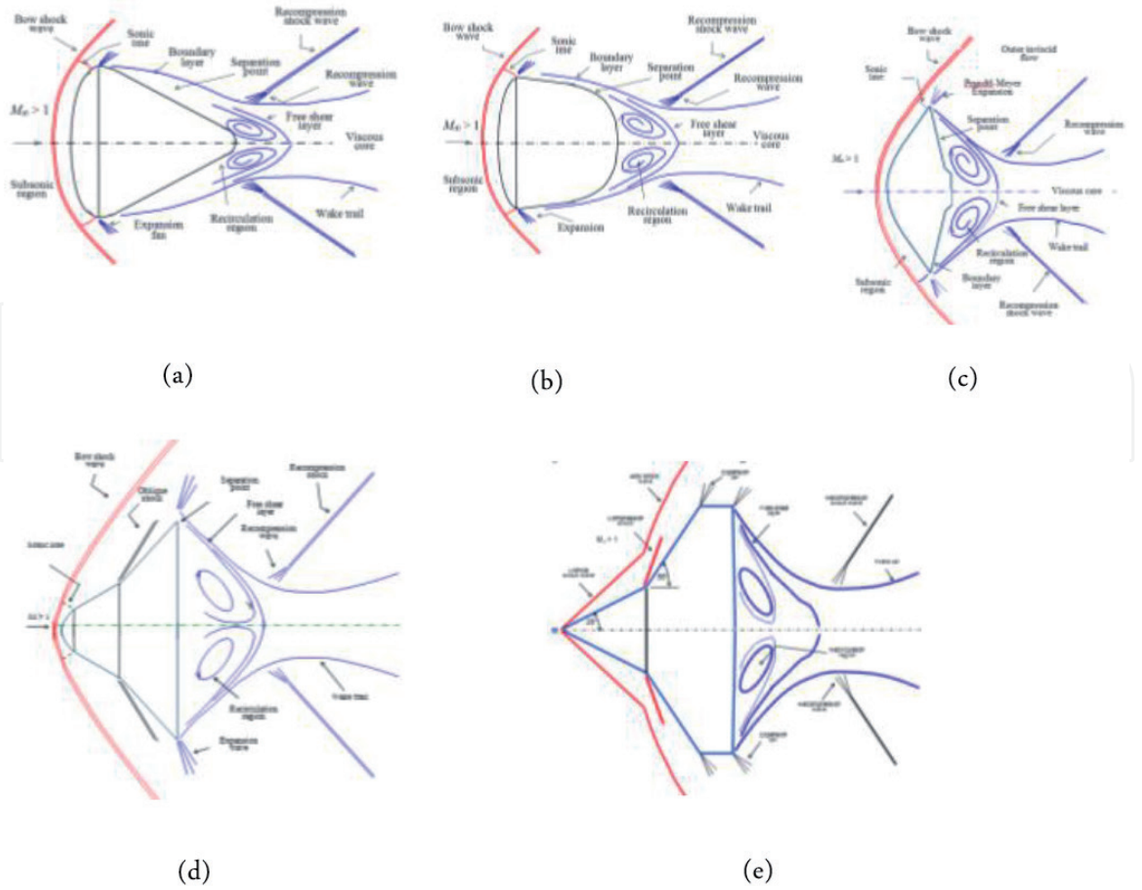

Figure 3.
Schematic sketches of flowfield over various reentry capsules (a) Apollo; (b) Soyuz; (c) OREX; (d) SRE; and (e) double-cone capsule.

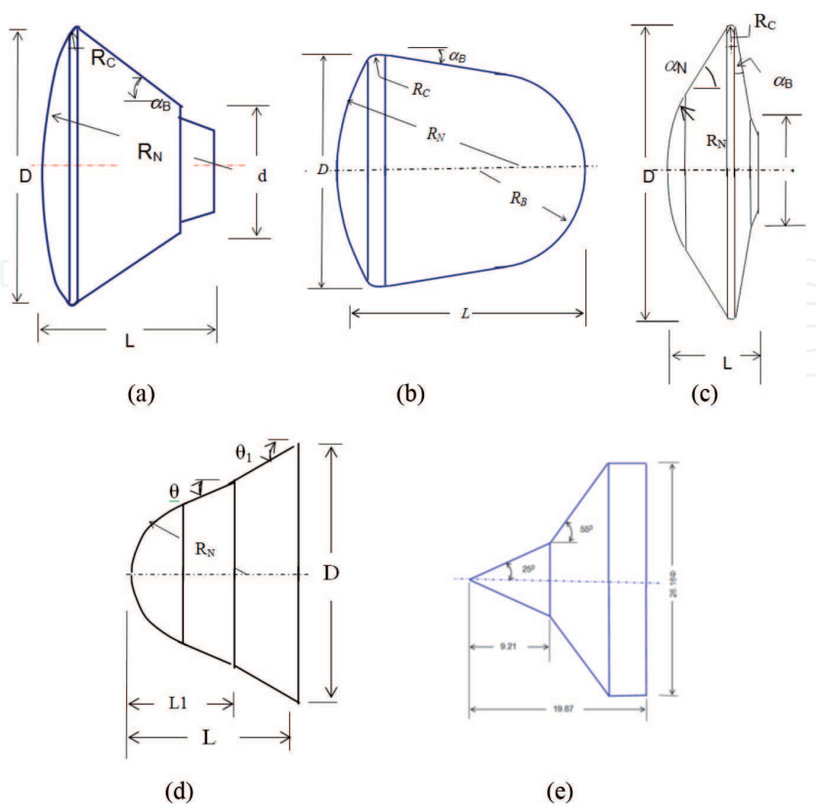

Figure 4.
Geometrical parameters of reentry capsules, (a) ARD; (b) Soyuz; (c) OREX; (d) SRE; and (e) double-cone space vehicles.

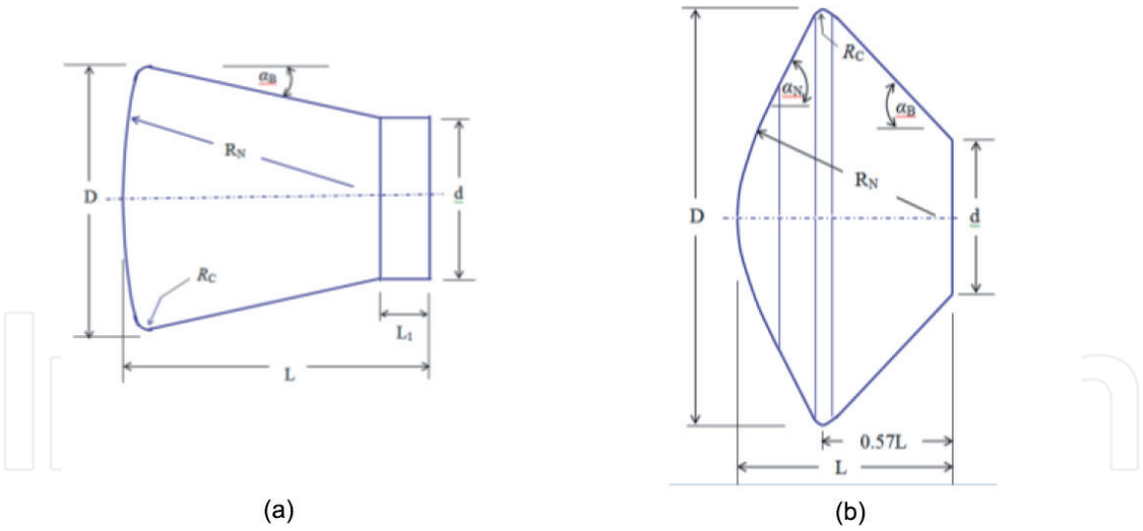

Figure 5.
Geometrical parameters of reentry capsules (a) CARINA; (b) Beagle-2.

Geometrical parameters	Capsules				
	Viking	MPF	MER	Phoenix	MSL
			α_N = 30°		
Fore-body diameter, *D*	3.5	2.65	2.65	2.65	4.5
DGB parachute diameter	16.4	12.4	15.09	11.5	19.7

Table 2.
Geometrical parameters of Viking, MPF, MER, Phoenix and MSL.

Capsule	R_N	D	R_C	L	α_N^0	α_B^0
ARD	3.36	2.80	0.014	2.04	—	33
Apollo-II	4.595	3.95	0.186	3.52	—	33
OREX	1.35	3.40	0.001	1.50	50	15
CARINA	1.97D	1.0D	0.25D	1.172D	—	13
MUSES-C	2.0	4.0	—	2.0	45	45
Beagle-2	41.7	90.0	0.029	49.95	60	43.75

Table 3.
Dimension of the reentry capsules.

Semi-cone angle	R_N	D	L_1	L
θ = 25°	3.36	2.80	0.014	2.04
θ = 30°	4.595	3.95	0.186	1.50
θ = 35°	1.35	3.40	0.001	1.50

Table 4.
Dimension of the blunted-spherical cone (SRE) reentry module.

The effects of the module geometrical parameters, such as radius of the spherical cap radius, shoulder radius, semi-cone angle and back-shell inclination angle on

the flowfield characteristics hence the base drag coefficient are analyzed which will provide a useful input for the optimization of the reentry module.

5. Numerical algorithm

5.1 Governing fluid equations

As discussed above the base pressure measurements in the wind-tunnel testing are affected by presence of sting attached to model. The free-flight data depend on quality of the transmitted telemetry data. The fluid dynamic equations describing the flowfield around a space vehicle include equations of continuity, momentum, and total energy. A numerical simulation of unsteady, compressible, axisymmetric laminar Navier-Stokes equations is an alternative to the expensive experimental testing of the reentry vehicles. The governing fluid dynamics equations can be written in the following conservation form in order to capture shocks and discontinuities as

$$\frac{\partial \boldsymbol{U}}{\partial t} + \frac{\partial \boldsymbol{F}}{\partial x} + \frac{1}{r}\frac{\partial (r\boldsymbol{G})}{\partial r} + \frac{\boldsymbol{H}}{r} = 0 \tag{3}$$

Temperature T is related to pressure and density by the perfect gas equation of state. The ratio of the specific heats γ is assumed constant and is equal to 1.4. The coefficient of molecular viscosity is evaluated in the flow solver employing Sutherland's formula. The flow is assumed to be laminar, which is consistent with experimental results of Cassanto [37] and Bulmer [42].

5.2 Numerical technique

To simplify the spatial discretization in numerical technique, Eq. (3) can be written in the integral form over a finite computational domain Ω with the boundary of the domain Γ as

$$\frac{d}{dt}\int_{\Omega} \boldsymbol{U} d\Omega + \int_{\Gamma} (\boldsymbol{F} dr - \boldsymbol{G} dx) + \int_{\Omega} \boldsymbol{H} d\Omega = 0 \tag{4}$$

The contour integration around the boundary of the cell is performed in anticlockwise sense in order to keep flux vectors normal to boundary of the cell. The computational domain Ω is having a finite number of non-overlapping quadrilateral cells. The conservation variables within the computational cell are represented by their average values at the cell centre.

The inviscid fluxes are computed at the centre of the cell resulting in flux balance. The summation is carried out over the four edges of the cell. The derivatives of primitive variables in the viscous flux are evaluated by using the method of lines. A system of ordinary differential equations in time is obtained after integrating Eq. (4) over a computational cell. In the cell-centered spatial discretization scheme is non-dissipative, therefore, artificial dissipation terms [55] are added by blending of second and fourth differences of the vector conserved variables. The blend of second and fourth differences provides third order back ground dissipation in smooth region of the flow and first-order dissipation in shock waves.

The spatial discretization described above reduces the integral equations to semi-discrete ordinary differential equations (ODE). The ODE is solved using multi-stage Runge-Kutta time stepping scheme of Jameson et al. [55]. The numerical algorithm is second-order accurate in space discretization and time integration.

The scheme is stable for a Courant number ≤2. Local time steps are used to accelerate to a steady-state solution by setting the time step at each point to the maximum value allowed by the local Courant-Friedrichs-Lewy (CFL) condition.

5.3 Initial and boundary conditions

The freestream conditions for each trajectory point are tabulated in **Table 5**, which are used as initial conditions. The freestream flow values are used to initialize the whole flowfield.

The boundary conditions are as follows: a no-slip condition and isothermal wall is considered as a solid wall boundary condition. At the inflow, all the flow variables are taken at the freestream values as tabulated in **Table 5**. A symmetry condition is imposed on the centre line upstream and downstream of the reentry vehicle. All variables are extrapolated at the outer computational boundary.

5.4 Computational grid

The body oriented grids are generated using a homotopy scheme. The stretched grids are generated in an orderly manner. The grid-stretching factor is selected as 5,

M_∞	p_∞, Pa	T_∞, K
1.2	4519	210
1.4	3952	213
2.0	2891	219
3.0	2073	224
5.0	1238	232
6.0	1064	234

Table 5.
Trajectory points and initial conditions.

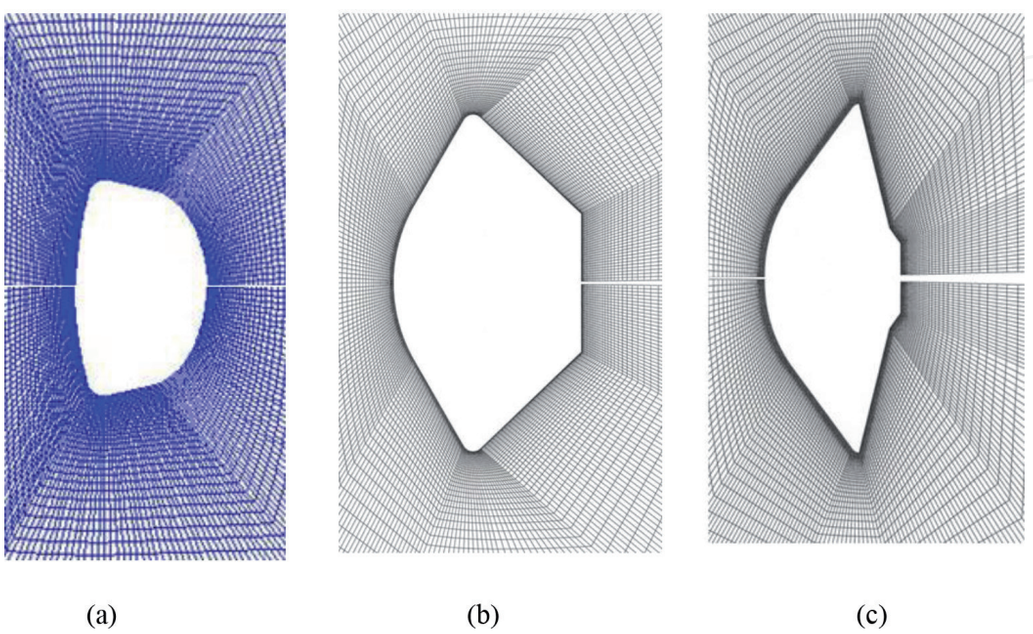

Figure 6.
Enlarged view of computational grid; (a) Soyuz; (b) MUSES-C; and (c) OREX.

and the outer boundary of the computational domain is maintained as 1.5–2.5 times maximum diameter D of the reentry module. In the downstream direction, the computational boundary is about 6–9 times the diameter of the module; D. **Figure 6** shows enlarged view of grid over the Soyuz, the MUSES-C and the OREX vehicle. The grid arrangement is found to yield a relative difference of about ±5% in the computation of fore-body aerodynamic drag coefficient. The convergence criterion is based on the difference in density values at any of the grid points, between two successive iterations $\left|\rho^{n+1} - \rho^{n}\right| \leq 10^{-5}$ where n is time-step counter. The present numerical algorithm is described in detail in Refs. [24, 25] and validated with many test cases.

6. Flowfield characteristics

Figure 7 depicts the velocity vector plots over the Apollo, the Apollo-II, the OREX and the MUSES-C space vehicles. It can be visualized from the vector plots that all the significant flowfield features such as a bow shock wave, rapid expansion fans at the shoulder, recirculation region with a converging free-shear layer and formation of the vortex flow in the base-shell region are well captured for M_∞ = 5.0. The wake flowfield immediately behind the space vehicle base exhibits complex flow characteristics. The formation of the bow shock wave on the fore-body

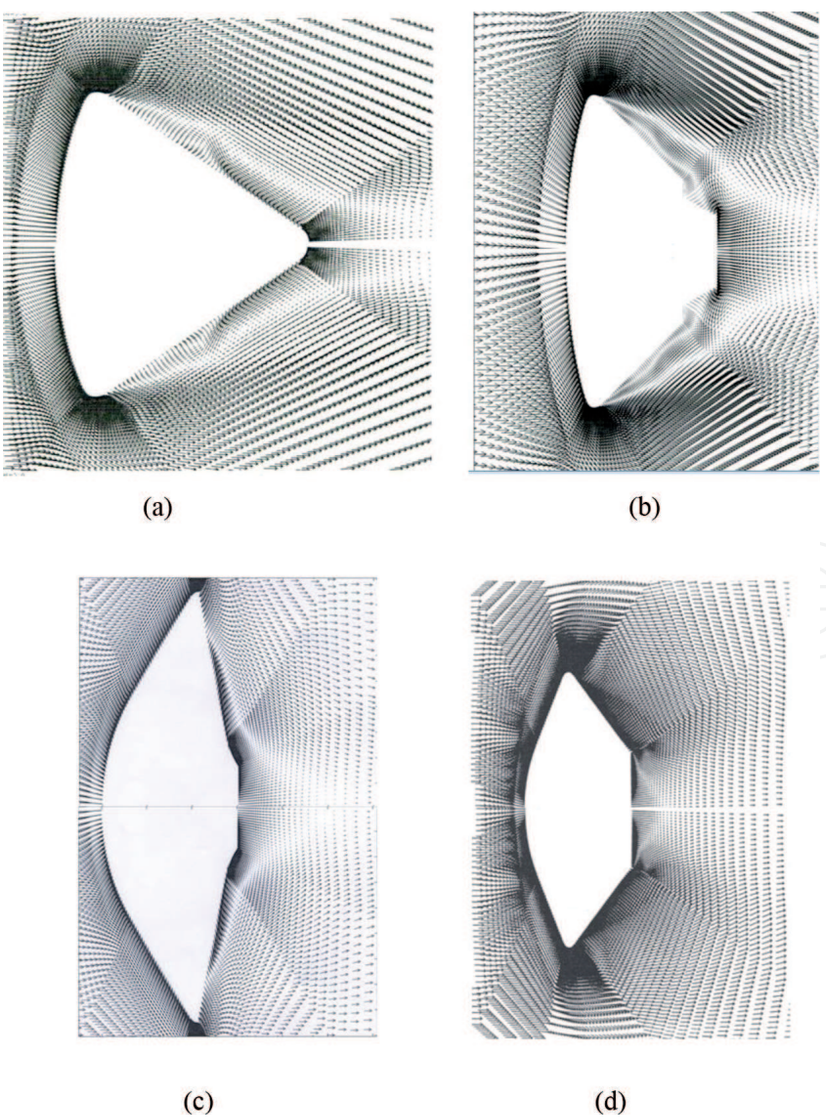

Figure 7.
Close-up views of velocity vector plots (a) Apollo; (b) ARD; (c) OREX and (d) MUSES-C at M_∞ = 5.0.

depends on R_N and α_N and M_∞. The bow shock wave moves close to the fore-body with the increasing M_∞ and the stand-off distance between the bow shock wave and the fore body decreases with the increasing M_∞. The Mach contour plots over the OREX and the MUSES-C are depicted in **Figure 8** for M_∞ = 1.2. The wake flowfield, immediately behind the capsule base, exhibits complex flow characteristics as observed in the vector plots.

Mach contours over the CARINA and Beagle-2 modules are exhibited in **Figure 9** for M_∞ = 1.2. The Mach contours over the SRE capsule for θ = 25° at M_∞ = 2.0 and 3.0 are shown in **Figure 10**. The bow shock wave does not follow the fore-body contour, which is due to small value of R_N and presence of semi-cone angle θ as compared to the OREX, the MUSES-C and the Apollo.

Figure 11(a) and **(b)** depicts velocity vector and Mach contour plots, respectively, over the double-cone (25/55°) configuration at M_∞ = 3. Despite its geometric simplicity, the double-cone shows the complex flowfield characteristics. A separation bubble can be observed on the vector plots. The separation and reattachment points are marked with the symbols "*S*" and"*R*"in the vector plots. It can also be seen from the vector plots that all the significant flowfield features are well captured such as the formation of conical shock wave on the tip, rapid expansion fan on the corner, recirculation region with converging free-shear layer and formation of the vortex flow in the aft region of the sharp-tipped double cone configuration.

The above numerical simulations over various reentry space capsules show that the separated flow can be found in the base region of the reentry capsules. The flow around the capsule is divided into two regions; inside and outside of the

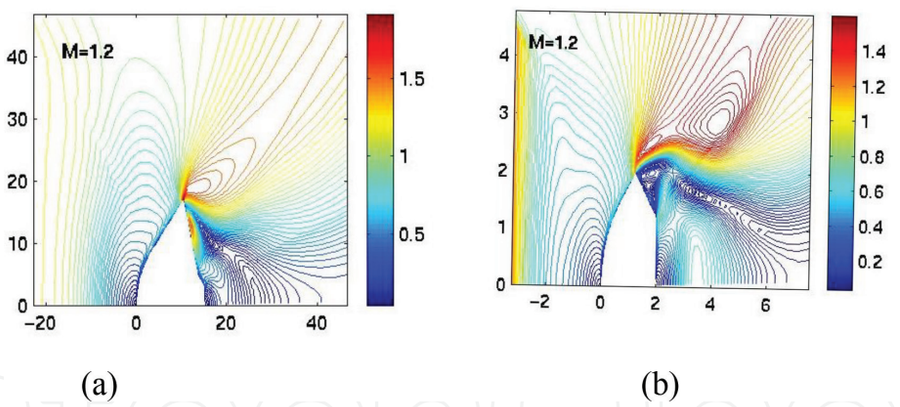

Figure 8.
Mach contours over capsules at M_∞ = 1.2 (a) OREX and (b) MUSES-C.

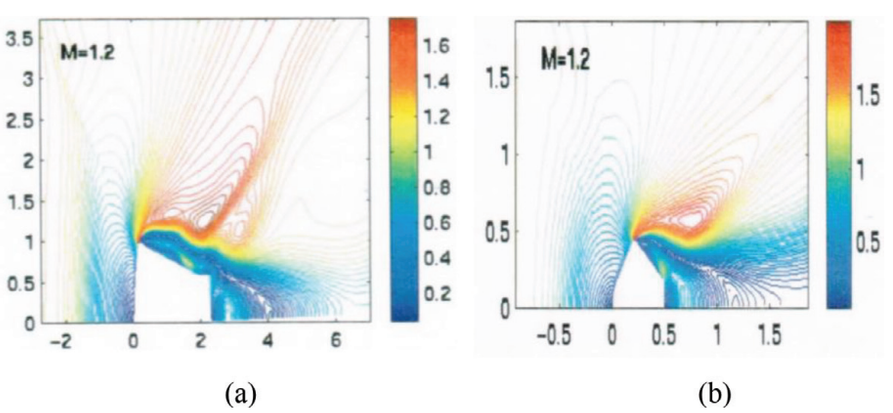

Figure 9.
Mach contours over (a) CARINA; and (b) Beagle-2 module at M_∞ = 1.2.

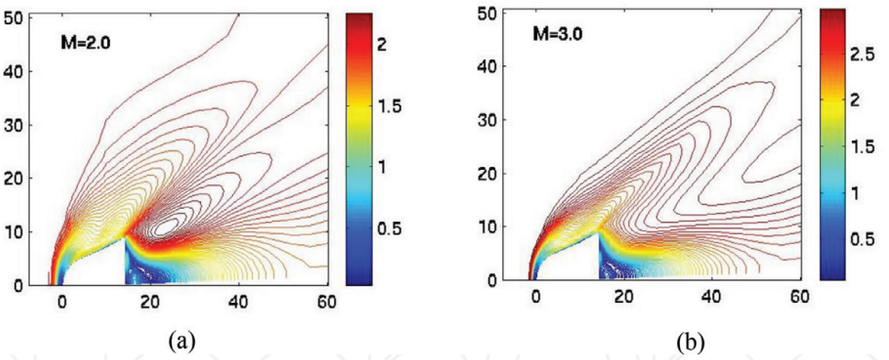

Figure 10.
Mach contour over SRE module at (a) M_∞ = 2.0 and (b) M_∞ = 3.0 at θ = 25°.

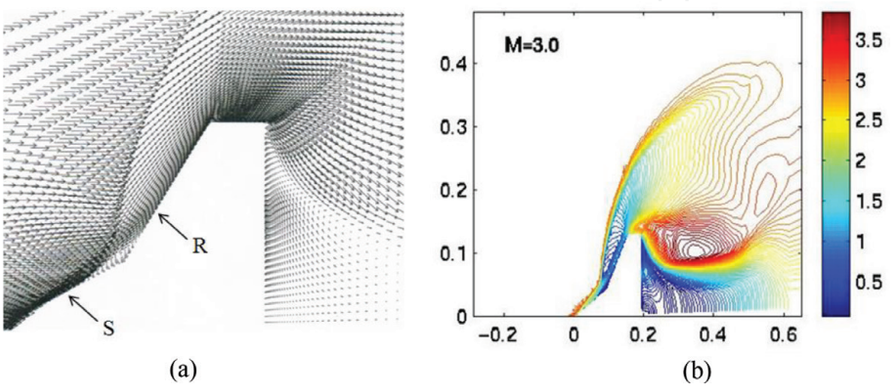

Figure 11.
(a) velocity vector and (b) Mach contours over double-cone module.

recirculation zone, and the shear layer separating the regions. The flowfield is very complex because of the back-shell. The wake flowfield, immediately behind the capsule base, exhibits vortex flow behavior. The formation of the bow shock wave on the fore body of the capsule depends on geometrical parameters such as spherical cap radius and the apex cone angle, and the value of the freestream Mach number. A low pressure is observed immediately downstream of the base which is characterized by a low-speed recirculating flow region, which can be attributed to filling-of the growing space between the shock wave and the reentry module. This flowfield behavior results the base drag.

Figure 12(a) and **(b)** depicts the variation of surface pressure coefficient *Cp* over the surface and the base plane, respectively, of the SRE capsule at M_∞ = 6.0, where *s* is measured along the surface of the fore-body. The *s* = 0 is the location of the stagnation point. The *Cp* variations is gradually decreasing over the spherical cap and remain nearly constant in the conical section of the SRE as depicted in **Figure 12(a)**. A sudden fall in *Cp* is seen on the sharp shoulder of the SRE. In the base region of the SRE, the Cp_B remains nearly linear variation on the base plane as seen in **Figure 12(b)**. The Cp_B is high on the corner due to presence of the expansion fan.

Figure 13(a) shows variation of *Cp* over the MUSES-C capsule at M_∞ = 3.0. A sudden drop in *Cp* is observed on the shoulder of the MUSES-C accompanied by a negative pressure coefficient *Cp*. The Cp_B is shown in **Figure 13(b)** for the MUSES-C space vehicle. The Cp_B remains near to a constant value on the base plane. It is important to mention here that the Cp_B variation is gradual attributed to beveled shape shoulder of the MUSES-C. Thus, the *Cp* and Cp_B variations over the SRE and the MUSES-C exhibit the influence of the geometrical parameters and freestream Mach number.

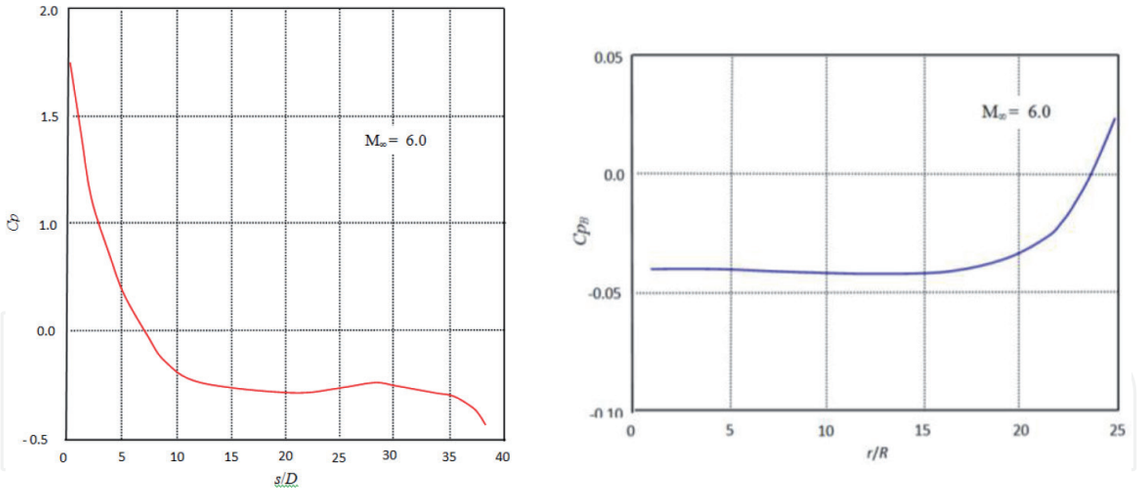

Figure 12.
Variation of pressure coefficient (a) over SRE module (b) on base region.

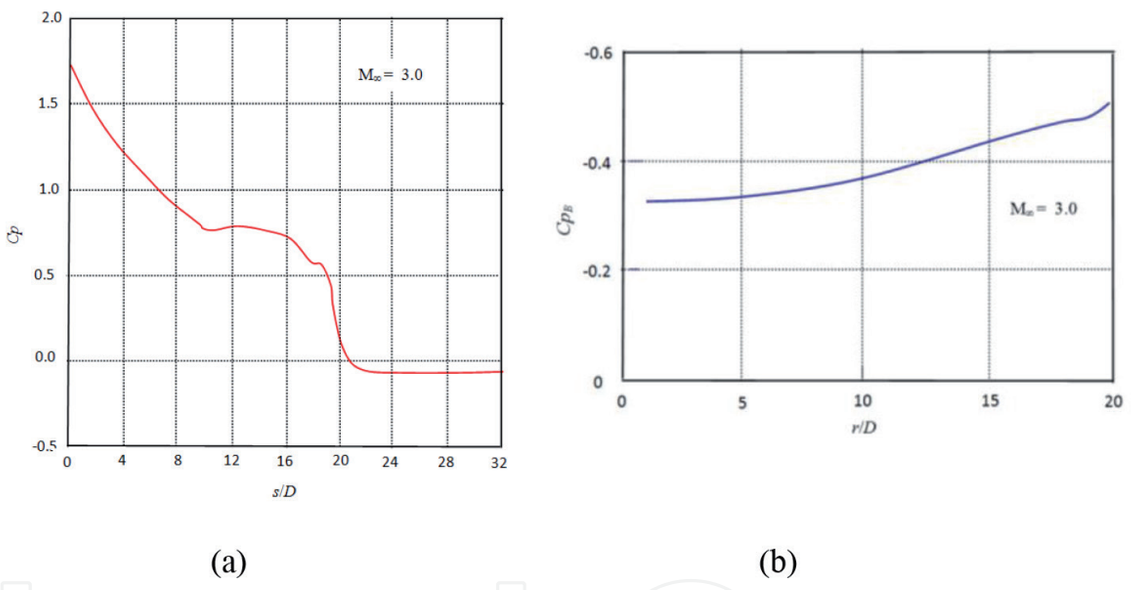

Figure 13.
Variation of pressure coefficient (a) over MUSES-C (b) on base region.

7. Base pressure and drag coefficients

Characteristics of flow features around the blunt body at supersonic speeds are described in the above section. The high surface pressure on the fore-body results in the high aerodynamic drag which is required for the aero-braking application. The base pressure coefficient can be calculated using following expression

$$C_{PBS} = \frac{(p_{BS} - p_\infty)}{\frac{1}{2}\rho_\infty V_\infty^2} \tag{5}$$

where subscript *BS* represents the base-stagnation point as depicted in **Figure 1(b)**. **Table 6** shows the computed base pressure coefficient C_{PBS} of the various capsules configurations at different freestream Mach numbers M_∞. **Table 6** shows OREX with smooth shoulder (beveled) and with a sharp corner. The C_{PBS} is high in the case of the OREX (S) as compared to the OREX with smooth shoulder. It again exhibits the effects of the shoulder shape geometry on the C_{PBS}.

Capsules	Cp_{BS}				
	M_∞ = 1.2	M_∞ = 2.0	M_∞ = 3.0	M_∞ = 5.0	M_∞ = 6.0
$Cp_{BS} = -2/(\gamma M_\infty^2)$	−0.9920	−0.7288	−0.3571	−0.1387	−0.0396
ARD	−0.5	−0.25	−0.15	−0.05	—
Soyuz	—	−0.50	−0.40	−0.20	—
Apollo	−0.30	−0.30	−0.20	−0.05	—
Apollo-II	−0.25	−0.30	−0.20	−0.08	—
OREX	−0.75	−0.30	−0.20	−0.10	—
OREX (S)	−0.90	−0.40	−0.25	−0.18	—
CARINA	−0.50	−0.30	−0.20	−0.05	—
MUSSES-C	−0.70	−0.30	−0.20	−0.10	—
Beagle-2	−0.8	−0.28	−0.15	−0.10	—
Double-cone, 25/55°	—	−0.25	−0.20	—	−0.05
SRE, θ = 25°	−0.82	−0.30	−0.20	—	−0.01
SRE, θ = 30°	−0.80	−0.32	−0.20	—	−0.01
SRE, θ = 35°	−0.70	−0.30	−0.20	—	−0.01

Table 6.
Pressure coefficient at base stagnation point of various reentry modules.

Capsule	C_{DB}				
	M_∞ = 1.2	M_∞ = 2.0	M_∞ = 3.0	M_∞ = 5.0	M_∞ = 6.0
OREX	-0.117×10^{-5}	-0.555×10^{-6}	-0.244×10^{-7}	-0.723×10^{-9}	
OREX (S)	-0.228×10^{-5}	-0.124×10^{-5}	-0.539×10^{-6}	-0.170×10^{-6}	
Carina	-0.389×10^{-4}	-0.649×10^{-5}	-0.978×10^{-5}	-0.162×10^{-5}	
Double cone	-0.268×10^{-3}	-0.606×10^{-4}	-0.337×10^{-4}	-0.200×10^{-3}	
MUSES-C	-0.261×10^{-4}	-0.512×10^{-5}	-0.245×10^{-5}	-0.196×10^{-5}	
Beagle-2	-0.790×10^{-5}	-0.430×10^{-5}	-0.210×10^{-5}	-0.710×10^{-6}	
SRE θ = 20°	-0.261×10^{-4}	-0.331×10^{-4}	-0.146×10^{-4}		-0.467×10^{-5}
SRE θ = 25°	-0.517×10^{-5}	-0.159×10^{-4}	-0.360×10^{-4}		-0.851×10^{-4}
SRE θ = 30°	-0.622×10^{-5}	-0.254×10^{-4}	-0.111×10^{-4}		-0.355×10^{-4}
SRE θ = 35°	-0.383×10^{-6}	-0.138×10^{-4}	-0.318×10^{-4}		-0.177×10^{-4}

Table 7.
Base drag coefficient on various reentry capsules.

The aerodynamic drag is influenced by the fore-body shape. The fore-body aerodynamic drag coefficient for various reentry configurations at high speeds is earlier computed and tabulated in Ref. [56]. After body drag C_{DB} is calculated by integrating the surface pressure coefficient variation excluding the fore-body of the reentry vehicle and can be expressed as

$$C_{DB} = \frac{2\pi \int_i (C_{PB})\, r_i \sin\psi dx}{A_{\max}} \tag{6}$$

where r and ψ are local radius and local inclination angle in the x-direction station i respectively. A_{max} is the maximum cross-sectional area of the reentry module. **Table 7** shows the base body aerodynamic drag C_{DB} for various reentry modules. The present numerical simulation will be validated in future with experimentally measured data in order to assess the error bands between them. The influence of geometrical parameters of the space reentry capsules and freetream Mach number on the base pressure coefficient and the base drag coefficient can be seen in **Tables 6** and 7.

8. Conclusions

A main aim of the Chapter is to analyze numerically the base pressure over space reentry vehicles at freestream Mach number range of 1.2–6.0. A numerical algorithm is described to solve compressible laminar axisymmetric Navier-Stokes equations over various reentry capsules. The flowfield over the capsule reveals the effect of the geometrical parameters on the base pressure and base drag coefficients. The CFD methods yield flowfields over space vehicles without the interference of the sting-model attachment in wind tunnel experiments. A low pressure is formed in the base region of the capsule which is characterized by a low-speed recirculation region which can be due to fill-up the growing space. The approaching boundary layer separates at the corner and the free-shear layer is formed in the wake region. The wake flow also shows a vortex attached to the corner with a large recirculation, which depends on spherical nose radius, apex cone angle, back-shell inclination angle and freestream Mach number.

Nomenclature

C_D	drag coefficient
C_P	pressure coefficient
D	fore-body diameter
d	adapter diameter
$\boldsymbol{F}$, $\boldsymbol{G}$	flux vectors
$\boldsymbol{H}$	source vector
L	overall length
M	Mach number
p	static pressure
t	time
$\boldsymbol{U}$	conservative variables in vector form
R_N	radius of sphere
R_C	radius of shoulder
x, r	coordinate directions
α_N	semi-cone angle of fore-body
α_B	semi-cone angle of back-shell
γ	ratio of specific heats
θ	semi-cone angle
ρ	density
Subscripts	
B	base
BS	base stagnation point
∞	freestream condition

Author details

Rakhab C. Mehta[1,2]

1 Department of Aeronautical Engineering, Noorul Islam Center for Higher Education, India

2 School of Mechanical and Aerospace Engineering, Nanyang Technological University, Singapore

*Address all correspondence to: drrakhab.mehta@gmail.com

References

[1] Cassanto JE. A base pressure experiment for determining the atmospheric pressure profile of planets. Journal of Spacecraft and Rockets. 1973;**10**(4):253-261

[2] Lamb JP, Oberkampf WL. Review and development of base pressure and base heating correlations in supersonic flow. Journal of Spacecraft and Rockets. 1995;**32**(1):8-22

[3] Kawecki EJ. Comparison of several reentry capsule base pressure correlation. Journal of Spacecraft and Rockets. 1977;**14**(5):284-289

[4] Terry J, Barber T. CFD and experimental study of an inflatable reentry vehicle model at Mach 3 conditions. Acta Astronautica. 2007;**61**:854-865

[5] Togiti V, Lüdeke H. Computation of supersonic base flow using detached eddy simulation. In: Tropea C, Jakirlic S, Heinemann HJ, Henke R, Hönlinger H, editors. New Results in Numerical and Experimental Fluid Mechanics VI. Notes on Numerical Fluid Mechanics and Multidisciplinary Design (NNFM). Berlin, Heidelberg, Germany: Springer; 2007. p. 96

[6] Walpot I. Numerical analysis of the ARD capsule in S4 wind tunnel. In: Proceedings of the 4th European Symposium on Aerothermodynamics for Space Applications. Capua, Italy: ESA; 2001. pp. 523-527

[7] Chester W. Supersonic flow past a bluff body with a detached shock. Journal of Fluid Mechanics. 1965;**1**:353-365

[8] Freeman NC. On the theory of hypersonic flow past plane and axially symmetric bluff bodies. Journal of Fluid Mechanics. 1956;**1**:366-387

[9] Lighthill MJ. Dynamics of a dissociating gas, part 1: Equilibrium flow. Journal of Fluid Mechanics. 1957;**2**:1-32

[10] Wood AW, Gnoffo PA, Rault DFG. Aerodynamic analysis of commercial experiment transport reentry capsule. Journal of Spacecraft and Rockets. 1996;**33**(5):643-646

[11] Yamamoto Y, Yoshioka M. CFD and FEM Coupling Analysis of OREX Aero-Thermodynamic Flight Data, AIAA 95-2087, 1995

[12] Ivanov NM Catalogue of Different Shapes for Un-Winged Reentry Vehicles, Final Report, ESA Contract 10756/94/F/BM, 1994

[13] Solazzo MA, Sansome A, Gasbarri P. Aerodynamic characterization of the Carina reentry module in the low supersonic regimes. In: Proceedings of the 2nd European Symposium on Aerothermodynamics for Space Vehicles. Noordwiik, The Netherlands: ESTEC; 1994. pp. 41-47

[14] Liever PA, Habchi SD, Burnell SI, Lingard JS. Computational fluid dynamics prediction of the beagle 2 aerodynamic data base. Journal of Spacecraft and Rockets. 2003;**40**(5):632-638

[15] Mehta RC. High speed flowfield analysis for satellite launch vehicle and reentry capsule. Journal of Magnetohydrodynamics, Plasma and Space Research. 2008;**15**(1):51-99

[16] Ross JC, Brauckmann GJ. Aerodynamic and Aeroacoustic Wind Tunnel Testing of the Orion Space Craft, AIAA 2011-3160, 2011

[17] Murphy KJ, Bibb KL, Brauckmann GJ, Rhode MN, Owens B, Chan DT, et al. Orion crew module aerodynamic testing. In: 29th AIAA Applied Aerodynamics Conference; 27-30 June

2011; Honolulu, Hawaii, USA, AIAA Paper 2011-3502. 2011

[18] Zhenmiz Z, Yunliancy D, Yi L, Tieliang Z. Shape optimization design method for the conceptual design of reentry vehicles. Acta Aeronautica et Astronautica Sinica. 2011;**32**(11):1971-1979

[19] Ali SA, Husain M, Qureshi MN. Effects of nose-bluntness ratio on aerodynamic performance for reentry vehicle. Journal of Space Technology. 2012;**1**(1):38-41

[20] Viviani A, Pezzella G. Aerodynamic and Aerothermodynamic Analysis of Space Mission Vehicles. Switzerland: Springer International Publishing A. G.; 2015

[21] Chen B, Zhan H, Zhou W. Aerodynamic design of a reentry capsule for high speed manned reentry. Acta Astronautica. 2015;**106**:160-169

[22] Weiland C. Aerodynamic Data of Space Vehicles. Germany: Springer-Verlag Berlin Heidelberg; 2014

[23] Mehta RC. Effect of geometrical parameters of reentry capsules over flowfield at high speed flow. Advances in Aircraft and Spacecraft Science. 2017;**4**(4):487-501

[24] Mehta RC. Numerical simulation of supersonic flow past reentry capsules. Shock Waves. 2006;**15**(1):31-41

[25] Mehta RC. Computational investigation of flow oscillation over reentry capsules. International Journal of Computational Fluid Dynamics. 2006;**15**(2):247-260

[26] Prabhu R, Stewart J, Theraja R. Shock Interaction Studies on a Circular Cylinder at Mach 16, AIAA Paper 90-0606, 1990

[27] MacLean M, Wadhams T, Holden M, Candler G. Integration of CFD and experiments in the CUBRC LENS shock tunnel facilities to understand the physics of hypersonic and hypervelocity flows. In: 4th Symposium on Integrating CFD and Experiments in Aerodynamics; 14-16 September 2009; Rhode-Saint-Genèse, Belgium: Von Karman Institute. 2009

[28] Wright MJ, Sinha K, Olejniczak J, Candler GV, Magruder TD, Smits AJ. Numerical and experimental investigation of double-cone shock interactions. AIAA Journal. 2000;**38**(12):2268-2276

[29] Cassanto JE, Rasmussen NS, Coats JD. Correlation of free-flight base pressure data for M =4 to M = 19. AIAA Journal. 1969;**7**(6):1154-1157

[30] Nieden PZ, Olivier H. Determination of atmospheric densities from reentry flight data. Journal of Spacecraft and Rockets. 2007;**44**(2):332-337

[31] Cassanto JE. Effects of cane angle and bluntness ratio on base pressure. AIAA Journal. 1965;**3**(12):2351-2352

[32] Cassanto JE. Base pressure results at M = 4 using free-flight and sting-supported models. AIAA Journal. 1968;**6**(7):1411-1414

[33] Noack RW, Lopez AR. Inviscid Flowfield Analysis of Complex Vehicles: Vol. 1 Description of Numerical Methods, Report SAND-0776/1; Sandia National Laboratory, 1988

[34] McWherter M, Noack RW, Oberkamf WL. Evaluation of boundary layer and parabolized Navier-stokes solutions for reentry vehicles. Journal of Spacecraft and Rockets. 1986;**23**(1):70-78

[35] Baum E, King HH, Denison MR. Recent studies of the laminar base flow region. AIAA Journal. 1964;**2**(9):1527-1534

[36] Cassanto JE. Ratio on base pressure. AIAA Journal. 1965;**3**(12):351-352

[37] Cassanto JE. Radial base-pressure gradients in laminar flow. AIAA Journal. 1967;**5**(12):2278-2279

[38] Cassanto JE, Mendelson RS. Local flow effects on base pressure. AIAA Journal. 1968;**6**(6):1182-1185

[39] Cassanto JE, Schiff J, Softley EJ. Base pressure measurements on slender cones with domed after bodies. AIAA Journal. 1969;**7**(8):1607-1609

[40] Cassanto JE. Full-scale flight test base pressure results for a blunt planetary entry probe configuration. Journal of Spacecraft and Rockets. 1971;**8**(9):996-998

[41] Zarin NE. Base pressure measurements on sharp and blunt 9° cones at Mach numbers from 3.50 to 9.20. AIAA Journal. 1966;**4**(4):743-745

[42] Bulmer BM. Flight-test base pressure measurements in turbulent flow. AIAA Journal. 1976;**14**(12):1783-1785

[43] Sammonds RI, Kruse RL. Viking Entry Vehicle Aerodynamics at M = 2 in Air and some Preliminary Test Data for Flight in CO_2 at M = 11, NASA TN D-7974, 1975

[44] Venkatapathy E, Palmer G, Prabhu DK. AFE Base Computations Including Base Heating Predictions, AIAA Paper 91-1372, 1991

[45] Gnoffo PA, Weilmuenster R, Braun RD, Cruz CL. Influence of sonic line location on Mars path finder probe aerothermodynamics. Journal of Spacecraft and Rockets. 1996;**33**(2):169-179

[46] Tam LT. LU-SGS Implicit Scheme for Reentry Flow Computation and Comparison with Aerodynamic Flight Data, AIAA 92-2671, 1992

[47] Menne S. Computation of non-winged vehicle aerodynamics in the low supersonic range. In: Proceedings of the 2nd European Symposium on Aerothermodynamics for Space Vehicles; 21-25 November 1994; Noordwiik, The Netherlands: ESTEC. 1994. pp. 73-78

[48] Otten HBA. Preliminary computational investigation on aerodynamic phenomena DELFT aerospace reentry test vehicle. In: The Proceedings of the 4th European Symposium on Aerothermodynamics for Allocations; 15-18 October 2001; Capua, Italy: ESA. 2001. pp. 207-213

[49] Savino R, Peterna D. Blunted cone-flare in hypersonic flow. Computers and Fluids. 2005;**34**(7):771-890

[50] Barnhardt MD. Modeling and simulation of high speed wake flows [Ph.D. dissertation]. USA: University of Minnesota; 2009

[51] Suzuki K, Abe T. Transonic, Supersonic and Hypersonic Wind-Tunnel Tests on Aerodynamic Characteristics of Reentry Body with Blunted Cone Configuration, Report No. 658; Kanagawa, Japan: The Institute of Space and Aeronautical Science, 1995

[52] Bedin AP, Mishin GI, Chistyakove MV. Experimental investigation of the aerodynamic characteristics and geometric parameters of flows about various molecular structures. In: Koptev YI, editor. Gas Dynamics. NY, USA: Nova Science Publishers; 1992. pp. 39-67

[53] Minenkol VE, Agafonov DN, Yakushev AG. Project analysis of aerodynamics configuration of reentry capsule shaped body based on numerical methods for Newtonian flow theory. Aerospace Scientific

Journal. 2015;**4**:1-14. DOI: 10.7463/aersp.0415.0813899. In Russian

[54] Stremel PK, McMullen MS, Garcia JA. Computational Aerodynamic Simulations of the Orion Command Module, AIAA 2011-3503, 2011

[55] Jameson A, Schmidt W Turkel E. Numerical Solution of Euler Equations by Finite Volume Methods Using Runge-Kutta Time-Stepping Scheme, AIAA Paper 81-1259, 1981

[56] Mehta RC. Aerodynamic Drag Coefficient for Various Reentry Configurations at High Speed, AIAA 2006-3179, 2006